

Lasers in Manufacturing Conference 2021

Spatter formation in high-speed laser processing of high-alloyed steel

Peter Hellwig^{a,*}, Klaus Schrickner^a, Jean Pierre Bergmann^a

^a Technische Universität Ilmenau, Production Technology Group, Gustav-Kirchhoff-Platz 2, 98693 Ilmenau, Germany

Abstract

The combination of high processing speeds and improved beam qualities enlarges the possible fields of laser applications enormously. Gas-free sheet cutting and precise mass corrections represent examples where spatter formation is applied as the primarily removal mechanism under the use of cw-mode laser radiation. For a deeper insight into spatter formation at processing speeds of several meters per second, the processing zone needs to be characterized in detail. In this study, a glass plate was used for flanking the processing zone to realize high-speed videography in a half-section setup. This approach allows performing measurements directly in the processing zone regarding several melt pool dimensions especially on inclination angle of the absorption front. In addition, high-speed records in a transmitted light mode were carried out to investigate spatter formation in more detail. Eventually, a mathematical model is developed that calculates the spatter radius depending on minimum and maximum flow velocity.

Keywords: high-speed videography; high-speed laser processing; spatter formation; loss of mass; spatter radius

1. Introduction

The fields of application for laser processes are growing constantly. Especially high processing speeds and improved beam qualities lead to applications ranging from welding to cutting. For example gas-free sheet cutting (Lütke, 2011) or precise mass corrections of metallic compounds can be realized when it comes to processing speeds of several meters per second. Precise mass corrections are necessary for balancing processes of high-speed turning rotors for example. The application of laser radiation instead of conventional chipping methods represents a novel approach in this context, when processing time can be shortened

* Peter Hellwig. Tel.: +49 3677 69 3866; fax: +49 3677 69 1660.
E-mail address: info@fertigungstechnik.de.

towards laser ablation. Spatter formation was identified as the primary removal mechanism when processing speeds of several meters per second are applied. The effect of spatter formation is well known from deep penetration laser welding at speeds beyond 8 m/min (Kaplan et al., 2011). Characterizations of the resulting processing zone have also been made in many studies to explain the phenomena of spatter formation (e.g. Schmidt et al., 2020). Regarding characterization of spatter formation and keyhole behavior, the application of X-ray imaging was used in Abt, 2018 to examine the formation of the keyhole up to welding speeds of 7 m/min. Tenner et al., 2017 took a different approach by observing the keyhole behind a glass plate in deep penetration laser welding of zinc coated steel with welding speeds up to 10 m/min. An increase of the welding speed up to 20 m/min already leads to huge enlargements of the keyhole in feed direction, which can be explained by the increased inclination of the keyhole front wall and the changed reflection conditions (Fabbro, 2010). When the welding speed is increased further to 50 m/min, it is referred to as an “absorption front” (Berger et al., 2013). Cunningham et al., 2019 could confirm the formation of the absorption front for processing speeds up to 70 m/min by means of high-speed-X-ray radiography. Investigations on remote laser cutting applications showed for processing speeds up to 840 m/min significantly reduced penetration depths and the formation of kerfs (Mahrle et al., 2009; Ullmann et al., 2013). In this context, the inclination angle of the absorption front has been determined by Musiol, 2015, via 3D-measurements of the solidified end crater after the laser processing.

In conclusion, it can be stated that many studies regarding the characterization and determination of several dimensions of the processing zone have been made for laser beam welding. Therefore, various methods were applied in a wide range of processing speeds. However, no detailed investigations on the processing zone especially the absorption front up to processing speeds of 600 m/min were conducted in-process. Investigations on high speed laser processing regarding the formation of the processing zone and the absorption front at speeds from 1 m/s (60 m/min) to 10 m/s (600 m/min) were carried out for this reason. A high-speed camera setup was developed that enabled the observation of the processing zone through a glass plate for this purpose. This method provides a better understanding of the resulting material removal mechanism at high processing speeds. Furthermore, a deeper knowledge of the inclination of the absorption front regarding the scanning speed was achieved by means of small focal diameters.

2. Experimental Setup

The experiments were carried out with stainless austenitic steel sheets 1.4301 (X5CrNi18-10; AISI 304) with a thickness of 3 mm. A 400 W fiber laser (TruFiber400, Trumpf Laser GmbH) was equipped with a galvanometric scanner (PFO 20, Trumpf Laser GmbH) in order to realize the relative motion between laser beam and work piece of up to 600 m/min. The beam was focused using a 135 mm focal distance F-theta lens. The technical data of the laser and scanning system are summarized in Table 1. The laser power was set to 380 W for all experiments.

Table 1. Technical data of the laser and scanning system

Technical data of laser and scanning system	Values
wavelength [nm]	1070
pulse repetition frequency	cw
focal diameter [μm]	16.5
BPP [$\text{mm} \cdot \text{mrad}$]	0.38
M^2	1.12
Rayleigh length [mm]	0.18
Focal length [mm]	135
max. scan speed [m/s]	600

A 5 mm thick glass plate was attached to the steel sheets, as depicted schematically in Fig. 1. Borosilicate glass was used for this setup because of its high thermal shock resistance and the low thermal expansion. For high-quality edges, the sheets were cut to size by wire-cut EDM. This ensures a minimum gap between the sheets and the glass plate during clamping. The challenge here was to place the laser focus with its small focal diameter of $16.5\ \mu\text{m}$ on the edge completely.

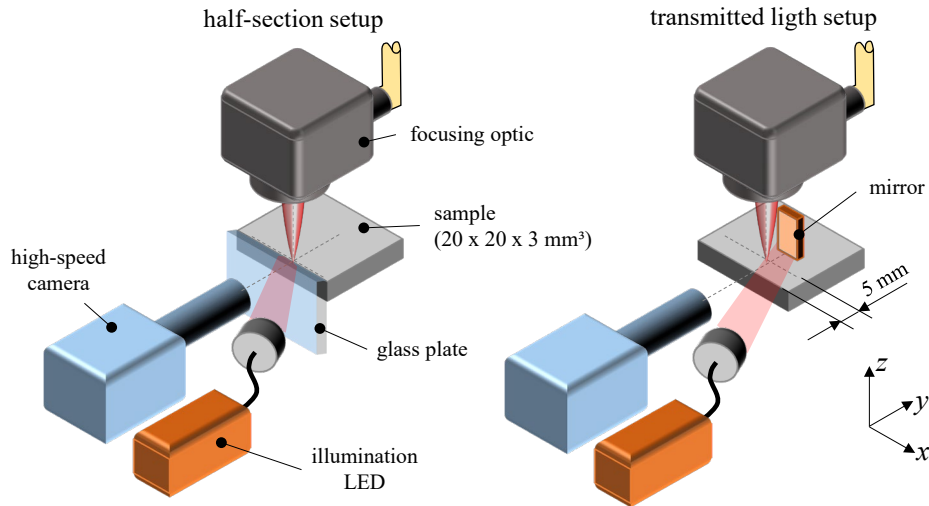


Fig. 1. Schematic depiction of half-section setup(left) and transmitted light setup (right) for high-speed records, (according to Hellwig et al., 2021)

To capture the processing zone, the high-speed camera Photron Fastcam SA-X2 (32 gigabyte internal memory, 1.8 seconds maximum recording duration) equipped with Navitar 12X ZoomLens objective was positioned perpendicular to the x-z plane (Fig. 1., left). The distance between camera lens and glass plate was about 100 mm. A narrow band filter for the wavelength of 630 nm was inserted into the optical path of the camera. The illumination was then realized with a high-power LED system with a corresponding wavelength. This setup allows to observe the evaporation front and the penetration depth during the process directly. A second setup (Fig 1, right) was applied, in order to capture the spatter detachment from the processing zone. For that purpose, a mirror reflected the light of the high-power LED directly into the optical path of the high-speed camera. This transmitted light mode makes the objects in the focal plane appear dark, while the background is lit very brightly. All records in this study were captured at a framerate of 150,000 fps.

In the following chapter the sample number n will be given in each diagram, while the error bars show the corresponding standard deviation. Furthermore, the processing speeds are given in meters per second.

3. Results and discussion

3.1. Characterization by Means of Half-Section Setup

In order to gain information about the dimensions of the processing zone, a half-section setup was developed in accordance with the work of (Tenner et al., 2017). The setup (see Fig.1) enabled a lateral view into the process. Fig. 4 shows some single snapshots at different times from a high-speed recording at a processing

speed of 1 m/s. The appearance of an almost vertically orientated keyhole can be observed for the shown example. The absorption front here even seems to be slightly inclined against the scanning direction. This phenomenon can be explained by a slight deviation in laser positioning in y-direction, which leads to the appearance of a solid area between the focal position and the glass plate. The absorption front was marked with a dotted line in the snapshots by connecting the assumed interaction position with the clearly visible ground of the resulting processing zone for this reason. Here, the assumed position of the incidence laser beam is marked with a red arrow in every single frame. Due to the small focal diameter of $16.5\ \mu\text{m}$, an exact indication of the position of interaction with the laser beam was very difficult to determine. However, the focal position could be determined in the records by means of a light reflection on the sheet surface. The half-section setup also enabled an observation of the melt flow, the metal vapour as well as the trailing area of solidification. To clarify the solidification line, a white dotted line is added to the snapshot for $+13.2\ \mu\text{s}$. Further, a really significant melt pool swelling is visible right behind the position of the incident laser beam and shows the direction of the up flowing melt.

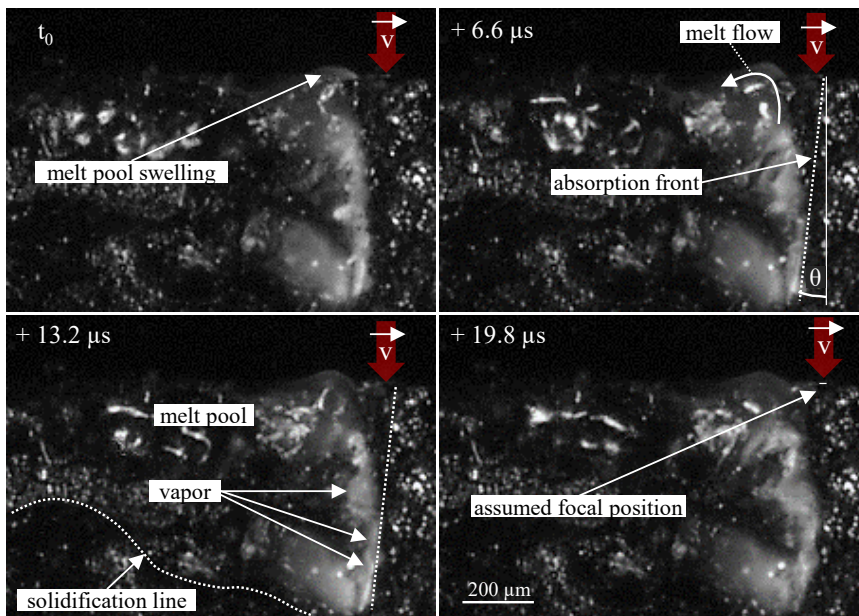


Fig. 2. Snapshots from a high-speed record in half-section setup at a processing speed of 1 m/s, (according to Hellwig et al., 2021)

The next step was to verify the transferability of the results from the half-section setup. The resultant penetration depths and seam widths from the half-section setup were compared with those from the cross-sections for all applied processing speeds for this purpose. This was used to directly show the difference that is caused by the changed thermal conditions. The results can be taken from Fig. 5. The penetration depths from the half-section setup were measured at three different times in each of the three high-speed records and correspondingly for nine single seams in cross-sections to calculate the mean values and standard deviations. The determination of the resulting seam widths was carried out correspondingly in cross-sections for nine single weld seams. The resulting seam width in half-section setup was measured afterwards in a top view by means of light microscopy.

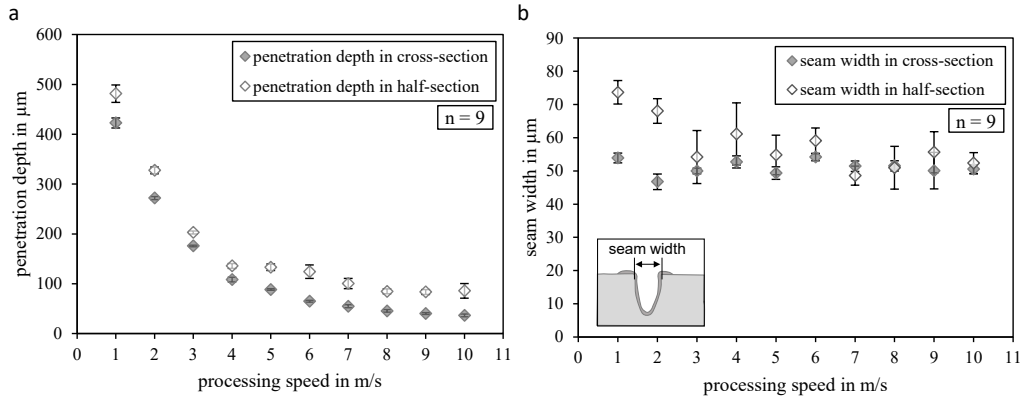


Fig. 3. Comparison of resultant dimensions in cross-section and half-section for: (a) penetration depth, (b) seam width, (according to Hellwig et al., 2021)

In Fig. 5a it can be seen that the penetration depth in cross-section were always lower than the values for the depth in half-section. Thereby, the difference between the results was significantly higher for 1 and 2 m/s processing speed. This effect can be explained by the larger heat accumulation resulting at the edge of the sample compared to the weld seams in cross-sections, which were produced with a distance of about 10 mm to the edge. The thermal conductivity of the glass plate is much lower compared to AISI 304, which led to a lower heat dissipation and correspondingly higher penetration depths. Regarding the results for the seam width in cross-section, it became obvious that the seam width could not clearly be influenced by the processing speed (see Fig. 5b). There was a plateau visible for the complete range of applied processing speeds. For the seam widths created using the half-section setup, increased values were only visible at 1 and 2 m/s. This might also have been caused by the higher amount of deposited heat at lower processing speeds. The high standard deviation for the data series of the seam width in half-section can be explained by small inaccuracies in the specimen-to-glass positioning. This effect occurs due to thermal expansions of the steel sheet and leads to small gaps between the glass plate and the sample.

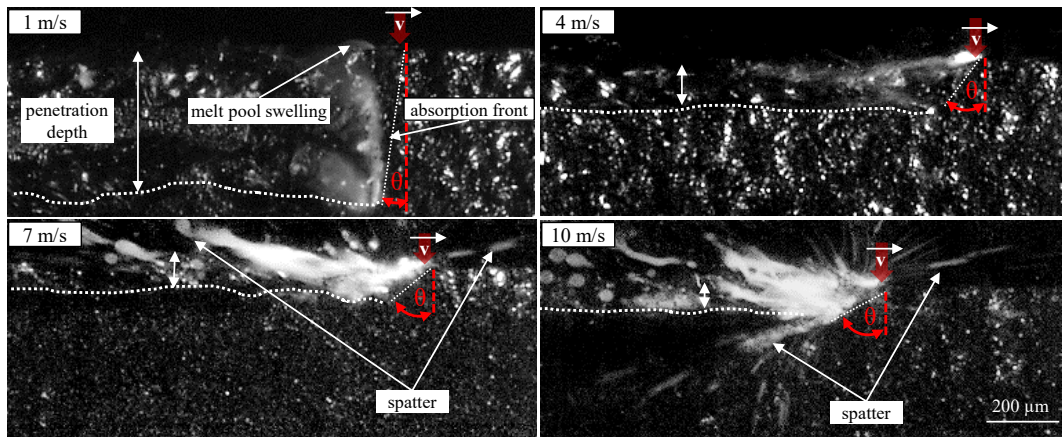


Fig. 4. Comparison of snapshots showing the resultant inclination angle of absorption front for different processing speeds, (according to Hellwig et al., 2021)

The differences depicted in Fig. 5 show that there is an influence of the half-section setup. However, the characteristics of the data are comparable. For this reason, the applied setup can be considered for valid investigations.

As already shown in Fig. 4, the half-section setup enables an observation of the absorption front and allows the measurement of its inclination angle. Therefore, Fig. 6 shows a comparison of snapshots of four selected processing speeds in half-section setup. At 1 m/s an almost vertical keyhole is visible. The melt pool swelling right behind the incident laser beam limits the keyhole aperture. At processing speeds beyond 4 m/s there are no trailing melt pool swellings visible. Beside the significant decrease of the penetration depth with increasing processing speed, the formation of spatters becomes evident at speeds beyond 7 m/s. A more detailed description based on these results was given in Hellwig et al., 2021.

The quantification of the resulting angles for the different applied processing speeds can be taken from Fig. 7a. The results show an almost linear relationship between the inclination angle of the absorption front and the processing speed. The values are rising almost continuously from about 14° at 1 m/s to 70° at 10 m/s. Thereby, the standard deviations show that there is no sudden transition between the applied processing speeds. A similar relationship between the processing speed and the inclination angle was already shown in Weberpals, 2010 for processing speeds in the range of 0.016 to 0.16 m/s and focal diameters from 200 to 600 μm .

A correlation of the inclination angle to the resultant loss of mass can be taken from Hellwig et al., 2021. There it could be shown that the loss of mass starts to increase significantly when the absorption front is inclined of about 60°.

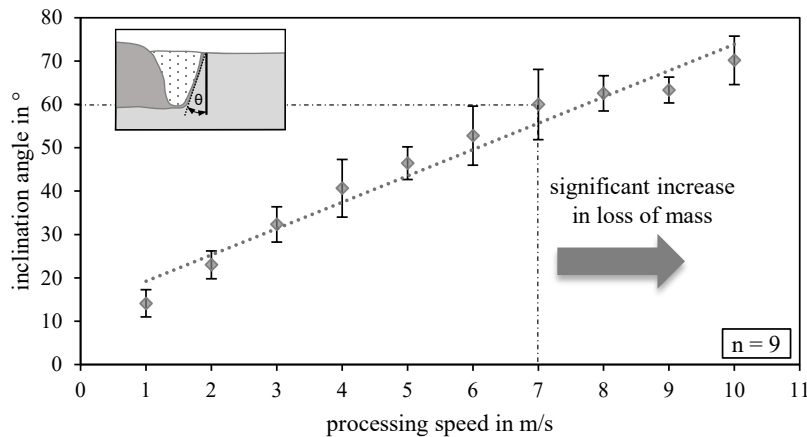


Fig. 5.(a) Resultant inclination angle of absorption front for different processing speeds, (according to Hellwig et al., 2021)

In order to investigate the effect of spatter detachment for the different processing speeds in more detail, the process was observed by means of a transmitted light setup (see Fig. 1., right). A comparison of single snapshots for each of the applied processing speeds is given in Fig. 6. Especially for 1 m/s, there can be seen huge weld pool swellings behind the interaction zone, like already shown in Fig. 4. These melt pool swellings also occurred at higher processing speeds from 2 to 5 m/s. In this case, they are only smaller and occurred further back, in an area that was not captured in the shown snapshots. By the comparison, it also becomes visible that a huge formation of spatters starts at a processing speed of 6 m/s. Below 6 m/s there can also be seen single spatter detachments. However, most of these single spatters could not be captured, since the pictures represent only snapshots. Furthermore, it can be observed that the angle of spatter detachment

increases with increasing processing speed. This leads to the assumption that the direction of the melt flow, respectively the direction of the spatter detachment is perpendicular to the absorption front, what was also shown in Ullmann et al., 2013. Regarding the size of the spatters, it becomes obvious that with increasing processing speed the size of the spatter decreases. However, it was not possible to carry out precise measurements at this point, due to the high velocity of the spatters and motion blur effects resulting from the light mode of the high-power LED illumination. For that reason, there are rather trajectories of the spatters visible especially for the higher processing speeds instead of clearly visible single spatters. Nevertheless, the snapshots can give a general overview regarding the resulting spatter size, amount and direction of detachment.

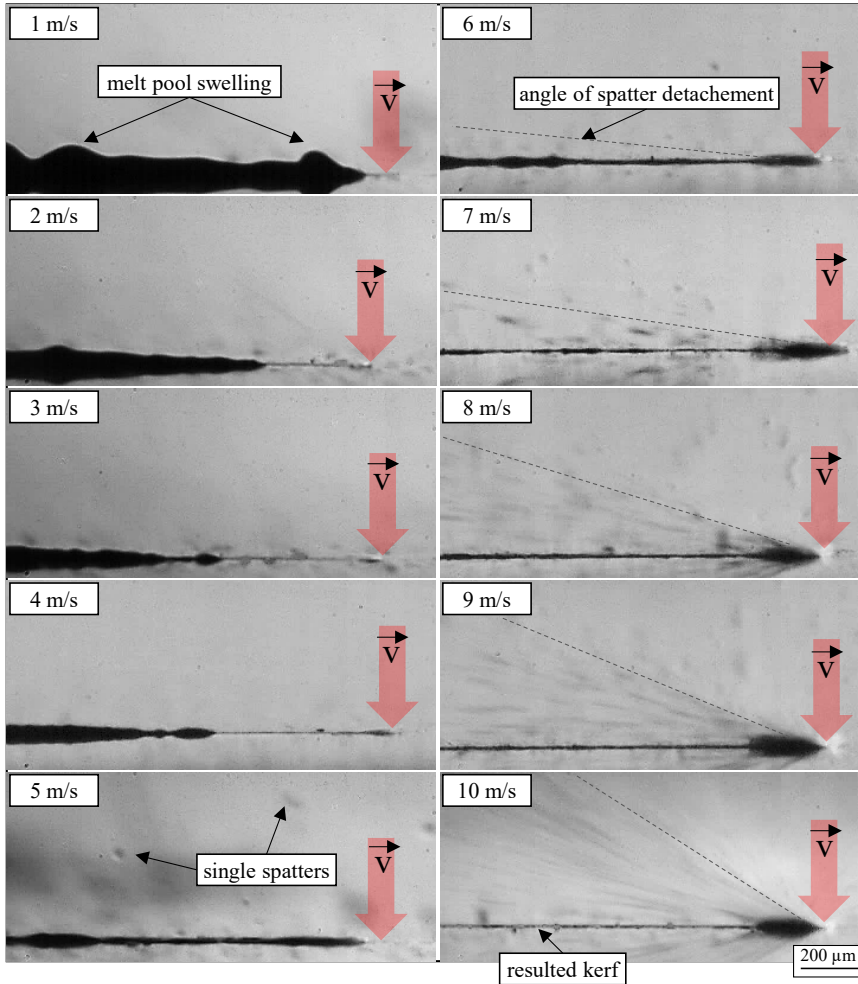


Fig. 6. Snapshots of high-speed records using the transmitted light setup

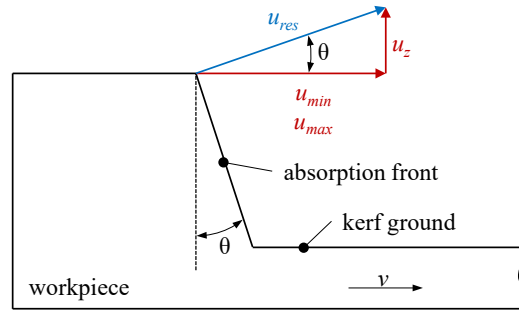
3.2. Model conception of spatter size

In section 3.1 it was indicated that the size of the spatters decreases with increasing processing speed. A relationship between processing speed and spatter size is presented based on this finding. For this purpose,

the considerations of Kaplan and Powell, 2011, on spatter formation during laser beam welding are utilized. Kaplan and Powell, 2011 provided a generally valid droplet escape condition given in equation (1) that depends on the vertical component of melt velocity u_z , melt density ρ , surface tension σ and resulting droplet radius R .

$$\rho u_z^2 > \frac{2\sigma}{R} \quad (1)$$

In case of laser processing with high speeds, it is assumed that the vertical flow component u_z is not decisive for spatter formation due to the fact that the melt flow is orientated perpendicular to the absorption front (see Ullmann et al., 2013). A resultant velocity u_{res} is assumed to be decisive for the spatter detachment for this reason. Fig. 7 depicts the assumptions for the resulting velocity u_{res} and its calculation by considering the inclination angle of the absorption front θ . Since estimation of flow velocities is challenging in general, two cases for minimum velocity $u_{res,min}$ (equation 2) and maximum velocity $u_{res,max}$ (equation 3) are considered.



$$u_{res,min} = \frac{u_{min}}{\cos \theta} \quad (2)$$

$$u_{res,max} = \frac{u_{max}}{\cos \theta} \quad (3)$$

Fig. 7. Model concept for calculating u_{res} depending the inclination angle of the absorption front

Taking into account both cases, a minimum as well as a maximum flow velocity around the absorption front must be determined. The relationship in equation (4) represents the maximum flow velocity around the keyhole according to Beck, 1996. Parameters considered are vaporization temperature T_v , melting temperature T_m , initial temperature T_0 , thermal diffusivity κ , keyhole diameter d_k (set to absorption front width) and processing speed v . The conditions are changed here compared to Beck, 1996, since a strongly elongated keyhole or an absorption front is present. Nevertheless, the approach can provide information on the maximum velocity. On the other hand, it is assumed that the minimum flow velocity is at least as fast as the processing speed (see equation 5). The Knudsen layer could become more important due to small melt layers in front of the absorption front, which must be taken into account with regard to the validity of the model. For simplification, however, this is not considered in the following.

$$u_{max} = v \left[1 + 2 \sqrt{\frac{1}{5} \left(\frac{T_v + T_m - 2T_0}{T_v - T_m} \right)^{\frac{5}{4}} \left(\frac{4\kappa}{v d_k} \right)^{\frac{3}{4}}} \right] \quad (4)$$

$$u_{min} = v \quad (5)$$

This model-based approach thus allows the determination of resulting spatter sizes regarding minimum and maximum velocities despite strong simplifications. This allows the basic characteristics to be derived with regard to the decrease in spatter size with increasing processing speed. u_{max} and u_{min} were utilized to get equation (6) and (7), respectively, to determine the minimum and maximum spatter sizes based on the considerations above.

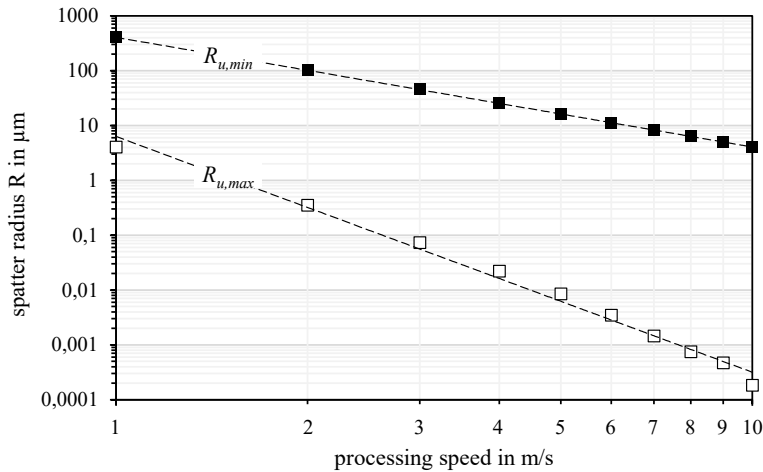
$$R_{u,max} < \frac{2\sigma}{\rho \frac{u_{max}^2}{\cos^2\Theta}} \quad (6)$$

$$R_{u,min} < \frac{2\sigma}{\rho \frac{u_{min}^2}{\cos^2\Theta}} \quad (7)$$

Fig. 8 shows the result of the model for the lower and the upper limit of flow velocity and resulting $R_{u,min}$ and $R_{u,max}$ on a double logarithmic scale. The principal shape of the curves shows a decreasing spatter size with increasing processing speed. It follows a power function in both cases, resulting in the representation of a straight line in the log-log plot. The considerations of the model thus confirm the experimental observations of decreasing spatter sizes with increasing processing speeds. The modeling actually addresses the behavior of the absorption front, i.e. effects of momentum, energy and mass transfer across the keyhole rear wall is not considered. However, the power function fit well even for lower processing speeds considered, e.g. 1 and 2 m/s. The consideration of $R_{u,min}$ and $R_{u,max}$ shows that flow velocity is decisive for resulting spatter sizes. Resulting spatter sizes are differing up to several orders of magnitude due to the different flow velocities.

The resulting window of spatter radii is relatively large, so further investigations will be carried out to determine the real spatter sizes as a function of processing speed. This allows the calibration of the model and, conversely, the determination of the present flow velocities.

Fig. 8. Spatter sizes calculated for u_{min} and u_{max} based on model conception



4. Conclusions

In this paper, investigations on high-speed laser processing of stainless steel AISI 304 for speeds from 1 m/s to 10 m/s have been evaluated in regard to spatter size. The use of a half-section setup enabled the processing zone to be observed and especially the inclination of the absorption front to be measured directly. The results for the inclination angle shows a nearly linear relationship to the processing speed, whereas at welding speed over 6 m/min a huge amount of spatter can be seen. With further process observations in a transmitted light setup decreased spatter radii with increased processing speeds can be concluded. Based on these findings, a mathematical model was developed, that calculates spatter radii depending on maximum and minimum flow velocity and inclination angle of the absorption front. Resulting spatter sizes are differing up to several orders of magnitude due to the different flow velocities, however, a power function describes spatter radii well in both cases. Further investigations will determine the real spatter size for a calibration of the developed model and may provide further information regarding flow velocities.

Acknowledgements

The authors gratefully acknowledge support and funding from the European Development Fund (EFRE) grant no. 2017 FE 9091.

Note

The data and figures (Fig.1 – Fig.5) in this conference paper were previously published in Hellwig et al., 2021 under the Creative Commons license CC BY 4.0 (<https://creativecommons.org/licenses/by/4.0/>). Adaptations were made regarding arrangements of individual figures to each other, the font of captions as well as the way of indicating the units.

References

- Abt, F., 2018. Bildbasierte Charakterisierung und Regelung von Laserschweißprozessen; Universität Stuttgart, PhD thesis.
- Beck, M., 1996. Modellierung des Lasertiefschweißens, B. G. Teubner Stuttgart, ISBN 3-519-06218-6
- Benyounis, K., Olabi, A., Hashmi, M., 2005. Effect of laser welding parameters on the heat input and weld-bead profile; Journal of Materials and Processing Technology., Seite 978–985.
- Berger, P., Hügel, H., 2013. Fluid Dynamic Effects in Keyhole Welding—An Attempt to Characterize Different Regimes; Phys. Procedia Vol. 41, Seite 216–224.
- Cunningham, R., Zhao, C., Parab, N., Kantzos, C., Pauza, J., Fezzaa, K., Sun, T., Rollett, A.D., 2019. Keyhole threshold and morphology in laser melting revealed by ultrahigh-speed X-ray imaging; Science 2019, vol. 363, Seite 849–852
- Fabbro, R. 2010. Melt pool and keyhole behaviour analysis for deep penetration laser welding; J. Phys. D Appl. Phys., Vol. 43
- Hellwig, P., Schricker, K., Bergmann, J.P., 2021. Investigations of the Absorption Front in High-Speed Laser Processing up to 600 m/min; Appl. Sci. Vol.11.
- Kaplan, A.F.H., Powell, J., 2011. Spatter in laser welding; J. Laser Appl., Vol. 23
- Lütke, M., 2011. Entwicklung des Remote-Laserstrahlschneidens Metallischer Werkstoffe; Fraunhofer-Verlag: Berlin, Germany.
- Mahrle, A., Lütke, M., Beyer, E., 2009. Fibre laser cutting: Beam absorption characteristics and gas-free remote cutting; J. Mech. Eng. Sci.Proc. Inst. Mech. Eng. Part C, Vol. 224, Seite 1007–1018.
- Musiol, J.D., 2015. Remote-Laserstrahl-Abtragschneiden; Herbert Utz Verlag: Munich, Germany. Volume 307.
- Schmidt, L., Schricker, K., Bergmann, J.P., Junger, C. 2020. Effect of Local Gas Flow in Full Penetration Laser Beam Welding with High Welding Speeds; Appl. Sci., Vol. 10.
- Tenner, F., Riegel, D., Mayer, E., Schmidt, M., 2017. Analytical model of the laser welding of zinc-coated steel sheets by the aid of videography; J. Laser Appl, Vol. 29.
- Ullmann, F., Loeschner, U., Hartwig, L., Szczepanski, D., Schille, J., Gronau, S., Knebel, T., Drechsel, J., Ebert, R., Exner, H., 2013. High-speed laser ablation cutting of metal; High-Power Laser Materials Processing: Lasers, Beam Delivery, Diagnostics, and Applications II; International Society for Optics and Photonics: San Francisco, CA, USA; Volume 8603.
- Weberpals, J.-P., 2010. Nutzen und Grenzen guter Fokussierbarkeit beim Laserschweißen, Universität Stuttgart, PhD thesis.